Proceedings of the ASME 2025 20th International Manufacturing Science and Engineering Conference
MSEC2025
June 23-27, 2025, Greenville, South Carolina

MSEC2025-155609

CONTACT-FORCE-BASED CLOSED-LOOP CONTROL OF MULTI-AXIS ADDITIVE MANUFACTURING WITH CONTINUOUS-FIBER-REINFORCED POLYMER

Yuexin Yang[1], Yi Zhou[1], Molong Duan[1,2,*]

[1]Hong Kong University of Science and Technology, Hong Kong SAR, China
[2]HKUST Shenzhen-Hong Kong Collaborative Innovation Research Institute, Futian, Shenzhen, China

ABSTRACT

Continuous fiber-reinforced polymer (CFRP) has outstanding properties of lightweight and exceptional mechanical performance. Additive manufacturing (AM) with CFRP is an automated process for fabricating complex and customized structures. Multi-axis CFRP-AM introduces an increased degree of freedom (DOF) and enables the depositing of continuous fibers on complex curved surfaces with freeform spatial trajectories, which have wide applications such as aerostructures and the automotive industry. However, this enhancement in capability also brings challenges of high complexity and printing quality. Furthermore, due to the inherent tensile properties of continuous fibers, depositing on a complex surface increases the possibility of printing defects. Fiber bridges, slippages, and abrasion are much easier to occur particularly for complex surfaces with concave features. Existing research efforts mainly adopt pretreatments such as path and motion planning to achieve a more precise and efficient printing process, while lacking the focus on the improvement of the manufacturing process, particularly the capacity to deal with uncertainties and high dynamics when printing on complex surfaces. Therefore, in this paper, we proposed a contact-force-based closed-loop multi-axis CFRP-AM system to improve the fiber depositing accuracy on closed-shell structures with concave surfaces. A trajectory generation method based on conformal mapping is established, enabling the fiber path design on a 2D map and angle-preserved mapping onto the 3D surface. The 3D fiber path on the curved surface is transformed into an executable printing trajectory with robot motion and printer extrusion planning, thereby establishing an environment conducive to closed-loop control. A proportional-derivative (PD) controller is adopted, and the real-time vertical contact force is exploited as a feedback signal to dynamically adjust the layer height between the nozzle and the printing surface. A material extrusion multi-axis CFRP-AM platform combining a co-extrusion nozzle, a 6-axes industrial robot, a six-degree-of-freedom load cell, and a real-time closed-loop control system is built to verify the proposed control framework. To showcase the enhancements in print quality enabled by closed-loop control, a representative revolution part featuring a concave surface is designed. Dry basalt continuous fiber is deposited using the established closed-loop multi-axis CFRP-AM system. The results indicate that vertical contact force is effectively maintained around the desired value throughout the printing process, ensuring robust adhesion between the deposited fiber and the surface. Notably, the incidence of printing defects, including fiber bridges, is markedly reduced through the implementation of contact force feedback control.

Keywords: Continuous fiber-reinforced composites, additive manufacturing, multi-axis, closed-loop control, contact force

1. INTRODUCTION

Continuous fiber-reinforced polymer (CFRP) composites have widespread industrial applications in aerospace, automotive, and architectural domains, owing to their remarkable attributes of lightweight construction, high stiffness, and superior strength [1]. In contrast to traditional fiber-reinforced material manufacturing methods such as winding, pultrusion, vacuum forming, co-weaving, powder impregnation, and compression processes, additive manufacturing (AM) presents a distinct advantage in producing intricately shaped components at a heightened level of automation [2].

Compared to the commonly used AM technologies for the fabrication of composite parts such as material extrusion, directed energy deposition, and laminated object manufacturing

* Corresponding author: duan@ust.hk

processes [3], material extrusion based CFRP-AM is the most widely used technology because of its low cost, strong operational capabilities, and high accuracy [4]. There are presently five distinct extrusion approaches including in situ impregnation, prepreg coextrusion, prepreg extrusion, in situ consolidation, and inline impregnation [5]. In-situ impregnation has the simplest setup which feeds dry fiber in a heated nozzle, where the fiber is impregnated with molten thermoplastic or thermoset resins before being extruded from the nozzle to construct a composite structure [6].

The continuous fiber embedded in the CFRP composites enables strength reinforcement along the deposition direction, and researchers have conducted studies on the optimization of fiber path distribution and orientation to effectively improve product performance and fiber utilization efficiency [7]. Due to the traditional layer-by-layer AM strategy, the deposited fibers are in a 2D plane, which limits the performance enhancement for complex structures. Multi-axis CFRP-AM based on robotic arms is advantageous in achieving more diverse fiber trajectories on a 3D surface, which significantly improves the ability to manufacture parts with complex geometries. Compared to traditional 2D plane stacking AM, multi-axis AM also shows the advantages in reducing the interlayer defects and step effects, decreasing additional support printing, and improving product performance and surface quality [8]. De Backer et al. [9] first developed a six-degree-of-freedom printing platform and successfully printed complex CFRP parts. Zhang et al. [10] also proposed a multi-axis CFRP-AM system to fabricate wound fiber parts and proved the strength improvement of CFRP-AM compared to the traditional flat-layer AM process.

The introduction of increased DOF numbers in multi-axis CFRP-AM leads to enhancement in capability, it also brings challenges of high complexity and influences on printing quality [11]. Unlike pure plastic material extrusion 3D printers, the continuous fibers will not melt. The tensioned fiber during the printing process has a higher possibility of defects when deposited on complex surfaces. Fiber bridges, slippages, and abrasion are easier to occur particularly for complex surfaces with concave features [12]. Existing research efforts mainly adopt pretreatments such as path and motion planning to achieve a more precise and efficient printing process [13], while lacking the focus on the improvement of the manufacturing process, particularly the capacity to deal with uncertainties and high dynamics when printing on complex surfaces.

Closed-loop control has been widely investigated in extrusion-based AM applications to enhance printing performances to maintain geometrical accuracy [14], nozzle condition [15], etc. The investigations of the closed-loop control of the CFRP-AM process are limited. Image in-situ monitoring [16] and contact-force-based control [17] have shown the efficiency of improving the printing quality of CFRP parts. Compared to image information with limited camera view angle, environment lighting variation, and heavy computation, contact forces have fast response and directly reflect the bonding condition between deposited fiber and platform, which has the advantage of being adopted as feedback control signals. Lee et al. [18] investigated the bonding between layers in CFRP and concluded that the normal pressure force contributes to intralayer adhesion. Zhang et al. [19] further classified the CFRP-AM process force into traction force, nominal force, ironing force, and viscous force to highlight the delicacy of the forces and their relationship to the printing quality. It has also been pointed out that the force acts as a desirable monitoring signal for potential CFRP defects [20].

In our previous work, contact forces during the CFRP-AM process are exploited as real-time feedback signals to control the feed velocity, layer height, and fiber extrusion rate [17]. The printing defects such as intralayer fiber misalignment and interlayer weak adhesion are obviously decreased with the application of force feedback control. Due to the limited 3-axis printing setup, the helical fiber path designed in the study is oriented along the cross-section direction while the fiber reinforcement along the axis direction is weak, which limits the wide application in complex structures. Multi-axis CFRP-AM provides the solution to fabricate freeform fibers on complex surfaces. However, printing on complex surfaces brings new challenges and printing defects such as fiber bridges may occur. Given the high complexity of multi-axis CFRP-AM, it is quite necessary to implement contact-force-based closed-loop control to help improve the printing performance, particularly in addressing intricate surface characteristics such as significant curvature and concave areas, an aspect that remains inadequately explored in current studies.

In this work, we aim to develop a closed-loop (CL) multi-axis CFRP-AM system with contact-force-based feedback (FB) control that enables printing on complex surfaces with concave features with improved quality. To generate a 3D fiber printing trajectory on complex surfaces for the robot-based multi-axis CFRP-AM system, a conformal-mapping-based method is proposed in Section 2. Section 3 introduces the implementation of a contact-force-based controller on concave surfaces. Section 4 shows the experiment details, including the hardware setup, multi-axis printed CFRP parts, and the case study of a part with concave surfaces, demonstrating the quality enhancement with the application of force feedback control, followed by the conclusion in Section 5.

2. FREEFORM FIBER PRINTING TRAJECTORY GENERATION ON COMPLEX SURFACE

2.1. Closed-shell structure with complex surface

Consider a continuous shell structure characterized by the continuous change of its cross-sections around a given center line. Define the center line as $\mathbf{x}_c(h):[0,H]\rightarrow\mathbb{R}^2$ where h is height along the build-up direction and the total height is H. With the centerline defined, the entire close structure is defined with the height-dependent cross-section function $\mathbf{c}_{s0}(l,h):[0,1]\times[0,H]\rightarrow\mathbb{R}^2$, where l is the percentage of the total length at each cross-section. The cross-section at height

h is defined in reference frames originated at $\mathbf{x}_c(h)$. Accordingly, the shell structure cross-section shape in the ground frame is given by

$$\mathbf{c}_s(l,h) = \mathbf{c}_{s0}(l,h) + \mathbf{x}_c(h). \tag{1}$$

Along each cross-section, l increases from 0 to 1 in a counterclockwise manner. This definition can be interpreted as an extension of the polar coordinate definition. Similar to the center line, the $\mathbf{c}_s(l,h)$ is assumed to be first-order continuous. The shell structure is assumed to be closed at each cross-section, satisfying

$$\mathbf{c}_s(0,h) = \mathbf{c}_s(1,h), \tag{2}$$

and curve $\mathbf{c}_s(0,h)$ formulates the spatial developing line. The tangential vector along the curve $\mathbf{c}_s(l,h)$ is expressed as

$$\mathbf{T}(l,h) = \frac{\mathbf{c}_s{}'}{\|\mathbf{c}_s{}'\|}. \tag{3}$$

2.2. 3D fiber path generation based on conformal mapping

The orientation of continuous fiber deposited on the complex surface plays an essential role in the reinforcement performance of the composite part. Directly generating fiber paths on complex surfaces is relatively challenging due to the computational complexity. In computer graphics, a surface is regarded as a 2D manifold with intrinsic nonzero curvature embedding in the three-dimensional Euclidean space. There exists a homeomorphic mapping $f:\mathscr{M}\to\mathscr{N}$ between the 3D surface $\mathscr{M}$ embedded in a flat 3D space and a 2D planar parameter domain $\mathscr{N}$. To generate printing paths on a complex surface, one strategy is to create printing paths in the 2D plane $\mathscr{N}$, and then use inverse mapping $f^{-1}:\mathscr{N}\to\mathscr{M}$ to obtain the 3D paths mapped on the complex surface for multi-axis printing [21].

This section presents the conformal parameterization of a free-form surface, which can conformally transform a complex 3D surface onto a regular 2D Euclidean plane (and vice versa) to facilitate the printing path design and trajectory generation. To map the closed-shell surface into a rectangle plane, the computational conformal mapping algorithm proposed by [22] is adopted, which minimizes the angular distortion and preserves the fiber reinforcement. Additionally, the landmark constraints are set to preserve the corresponding geometric features, which facilitates fiber path generation. The mapping procedure is described as follows, shown in FIGURE 1: according to the Riemann mapping theorem, most simply connected regions can be mapped conformally in a one-to-one way onto the open unit disk on the complex plane [23]. The $\mathscr{M}$ is firstly mapped to a planar unit disk by a quasi-conformal mapping $h:\mathscr{M}\to\mathscr{I}$, which is obtained by solving the partial differential equation

$$\begin{cases} \Delta h = 0, \text{ on } \mathscr{M} \\ h(\partial\mathscr{M}) = \partial\mathscr{I} \end{cases}, \tag{4}$$

where Δ is the Laplace-Beltrami operator defined on surface $\mathscr{M}$. Quasi-conformal mapping is a generalization of conformal mapping with bounded distortion, which satisfies Beltrami equations in complex form

$$\frac{\partial h}{\partial\mathscr{S}} = \mu_h(\mathscr{M})\frac{\partial h}{\partial\mathscr{M}}, \tag{5}$$

where μ_h is a given complex variable with $\|\mu_h\|_\infty < 1$ and referred to as the Beltrami coefficient of h, which characterizes the distortion of the mapping from conformality. Donate the Beltrami coefficient of the inverse mapping of h by $\mu_{h^{-1}} = \rho + i\tau$, define (x,y) as coordinates on the unit disk $\mathscr{S}$, $u = u(x,y)$, $v = v(x,y)$ are the corresponding coordinates on rectangular planar $\mathscr{N}$. The $\mathscr{S}$ is mapped to $\mathscr{N}$ with quasi-conformal mapping $g:\mathscr{S}\to\mathscr{N}$ by solving the generalized Laplace equations given by

$$\begin{cases} \nabla\cdot(\mathbf{A}(\nabla u)) = 0 \\ \nabla\cdot(\mathbf{A}(\nabla v)) = 0 \end{cases}, \tag{6}$$

$$\mathbf{A} = \begin{bmatrix} \alpha_1 & \alpha_2 \\ \alpha_2 & \alpha_3 \end{bmatrix},\ \alpha_1 = \frac{(\rho-1)^2+\tau^2}{1-\rho^2-\tau^2}, \quad \alpha_2 = \frac{2\tau}{1-\rho^2-\tau^2},\ \alpha_3 = \frac{(\rho+1)^2+\tau^2}{1-\rho^2-\tau^2}, \tag{7}$$

where $\nabla(\cdot) = [\partial(\cdot)/\partial x, \partial(\cdot)/\partial y]^\top$. Therefore, the conformal mapping $f:\mathscr{M}\to\mathscr{N}$ is established as $f = g\circ h$. Assume that the lateral surface of a closed-shell structure is an open surface connected by a developing line, the two vertexes of the developing line are selected as landmark constraints and mapped to the four corners of the 2D parametric rectangular plane, shown in FIGURE 1, with the landmark-matching Teichumuller mapping algorithm shown in [22].

The continuous surface defined in Section 2.1 is triangularly meshed into discrete points, represented by $\mathbf{S} = (x,y,z)$. For a triangle element i on the surface, the three nodes $\mathbf{p}_{i,1}$, $\mathbf{p}_{i,2}$, $\mathbf{p}_{i,1}$ are connected in the counterclockwise direction. The normal vector of the surface at triangle i is calculated by

$$\mathbf{N}(i) = \frac{(\mathbf{p}_{i,2}-\mathbf{p}_{i,1})\times(\mathbf{p}_{i,3}-\mathbf{p}_{i,1})}{\|(\mathbf{p}_{i,2}-\mathbf{p}_{i,1})\times(\mathbf{p}_{i,3}-\mathbf{p}_{i,1})\|}. \tag{8}$$

The 2D rectangle plane $\hat{\mathbf{S}}$ is obtained by conformal mapping f developed by curve $\mathbf{c}_s(0,h)$, and also formulated by discrete triangle elements. Define the fiber path in the 2D rectangular plane as $\hat{\mathbf{P}}(l): l \in [0,1] \rightarrow \mathbb{R}^2$ and l is the percentage of the total length. The $\hat{\mathbf{P}}(l)$ can be conformally mapped to $\mathbf{P}(l) \in \mathbb{R}^3$ by

$$\mathbf{P} = f^{-1}(\hat{\mathbf{P}}) = [P_x \quad P_y \quad P_z]^\top. \tag{9}$$

The curve length of the 3D fiber path is given by

$$s(l) = \int_0^l |d\mathbf{P}| = \int_0^l \left|\frac{\partial \mathbf{P}(l)}{\partial l}\right| dl. \tag{10}$$

Note that the curve length $s(l)$ monotonically increases based on the definitions, which indicates l and s formulate a one-to-one projection. Thus, the curve length parameterized fiber path is obtained and expressed by $\mathbf{P}(s)$.

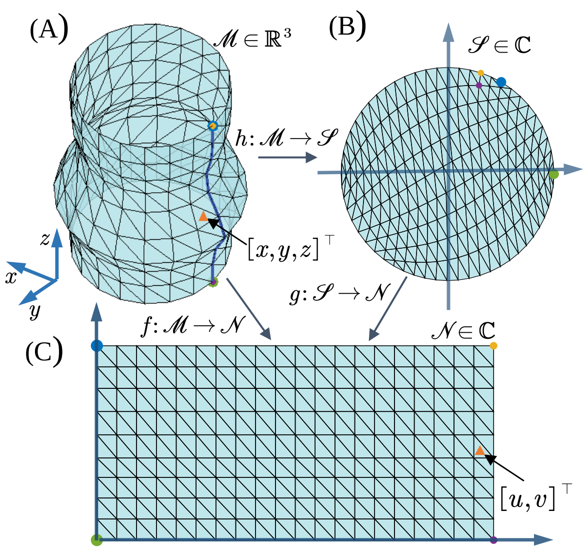

FIGURE 1: CONFORMAL MAPPING FROM A) 3D SURFACE TO 2D B) UNIT DISK, AND C) RECTANGLE

A criterion of an arbitrary point $\hat{\mathbf{P}}$ inside or on the triangle is determined with the following conditions [24]:

$$(\hat{\mathbf{P}} - \mathbf{p}_{i,k}) \times (\mathbf{p}_{i,k+1} - \mathbf{p}_{i,k}) \geq 0, k = 1, 2, 3, \tag{11}$$

where $\mathbf{p}_{i,k+1} = \mathbf{p}_{i,1}$. Based on the aforementioned criterion, the unique element number corresponding to each point on the fiber path can be identified, thereby enabling the determination of the normal vector $\mathbf{N}_0(s)$ of the surface at the current position. For each point on the fiber path, the tangential vector along each cross-section is calculated by Eq.(3) and expressed as

$$\mathbf{T}(s) = \mathbf{T}\left(\frac{\operatorname{atan}(P_y/P_x)}{2\pi}, P_z\right). \tag{12}$$

Then, the binormal vector $\mathbf{B}(s)$ is derived by

$$\mathbf{B}(s) = \frac{\mathbf{T} \times \mathbf{N}_0}{\|\mathbf{T} \times \mathbf{N}_0\|}. \tag{13}$$

Generally, $\mathbf{T}$ and $\mathbf{N}$ are not always orthogonal, the normal vector can be modified to

$$\mathbf{N}(s) = \mathbf{B} \times \mathbf{T}. \tag{14}$$

2.3. Multi-axis printing trajectory generation

Considering the multi-axis printing process shown in FIGURE 2, the printing part with complex surface is connected and fixed to the end-effector. The fiber path $\mathbf{P}(s)$ is transformed to fiber depositing position, also called workpiece position, by

$$^E\mathbf{P}_w = \mathbf{P} + \mathbf{P}_0, \tag{15}$$

where $\mathbf{P}_0$ is the initial printing position from the end-effector and the superscript ^{E} represents $^E\mathbf{P}_w$ is defined in the end-effector reference frame $\mathcal{F}_E$. To guarantee sufficient contact between deposited fiber to the surface, and avoid collision between the nozzle and complex surface, the local surface's normal direction should align with the vertical build orientation, as shown in FIGURE 2. Thus, the orientation of the workpiece is defined as

$$^E\mathbf{O}_f = {}^E\mathbf{R}[\mathbf{T}, \mathbf{N}, \mathbf{B}], \tag{16}$$

where $^E\mathbf{R}$ is the constant rotation matrix to transform the geometry model to frame $\mathcal{F}_E$ and $^E\mathbf{O}_f$ varies during the printing process. The nozzle position and orientation are defined in the ground reference frame $\mathcal{F}_G$, expressed by $^G\mathbf{P}_n$ and $^G\mathbf{O}_n$, respectively, which remain constant during the whole printing process and obey the following relationship:

$$\begin{cases} {}^G\mathbf{O}_n = {}^G\mathbf{O}_e {}^E\mathbf{O}_f \\ {}^G\mathbf{P}_n = {}^G\mathbf{P}_e + {}^G\mathbf{O}_e {}^E\mathbf{P}_w \end{cases}, \tag{17}$$

where $^G\mathbf{P}_e$ and $^G\mathbf{O}_e$ are the position and orientation of the robot end-effector, which are calculated by

$$\begin{cases} {}^G\mathbf{O}_e = {}^G\mathbf{O}_n {}^E\mathbf{O}_f^{-1} \\ {}^G\mathbf{P}_e = {}^G\mathbf{P}_n - {}^G\mathbf{O}_n {}^E\mathbf{O}_f^{-1E}\mathbf{P}_w = [P_{ex} \quad P_{ey} \quad P_{ez}]^\top \end{cases}. \tag{18}$$

Assume the depositing velocity as V_p, the curve length with respect to time t is obtained by

$$s(t) = V_p t. \tag{19}$$

The time-domain position ${}^{G}\mathbf{P}_e(t)$ and orientation ${}^{G}\mathbf{O}_e(t)$ of the robot end-effector in each time step t_s are thus derived. The ${}^{G}\mathbf{P}_e$ and ${}^{G}\mathbf{O}_e$ are used for inverse kinematic (IK) calculation to obtain the joint angles of the robot arm for execution. For any configuration of the 6-axes robot arm, the joint angles can be calculated by the mathematical method based on the robot arm's structure, and the solution is expressed as

$$\boldsymbol{\theta} = [\theta_1, \theta_2, \theta_3, \theta_4, \theta_5, \theta_6]^{\top}. \tag{20}$$

Generally, the calculated results from the IK solver consist of multiple solutions. To guarantee the robot arm executes a continuous and smooth motion, the best solution is selected by minimizing the distance between the current posture and the next posture, shown as

$$\boldsymbol{\Theta} = arg\min\left(\sum_{i=1}^{6} w_i \|\theta_i - \theta_i^*\|\right),\ \theta_i \in \hat{\boldsymbol{\Theta}}, \tag{21}$$

where θ_i^* represents the current joint angles of the robot arm, w_i represents the weight and $\hat{\boldsymbol{\Theta}}$ represents the joint limits. In addition, due to the amplification effect of robot configuration, even a tiny variation of orientation on the workspace could induce a large rotation of robot joints, resulting in huge joint velocities. Large joint velocities may lead to low moving accuracy with tracking errors and influence the printing quality. To minimize this error, a proxy fault signal u_v is constructed as

$$u_v = \begin{cases} \max\left\{\left|\dot{\boldsymbol{\Theta}}\right| - \dot{\boldsymbol{\Theta}}_{\max}\right\} & \text{when } \left|\dot{\boldsymbol{\Theta}}\right| > \dot{\boldsymbol{\Theta}}_{\max} \\ 0 & \text{when } \left|\dot{\boldsymbol{\Theta}}\right| \le \dot{\boldsymbol{\Theta}}_{\max} \end{cases}, \tag{22}$$

where $\dot{\boldsymbol{\Theta}}$ is joint velocity and $\dot{\boldsymbol{\Theta}}_{\max}$ is the maximum allowable joint velocity. It is desirable to design a feedback mechanism that minimizes the printing speed which is conveniently realized by a first-order system given by

$$\delta\dot{V} = -\frac{\delta V}{T_v} + b_v u_v, \tag{23}$$

where T_v is the time constant for the velocity regulation, b_v is the weight affecting the strength of the velocity reduction. With this definition, the actual printing velocity of the motion platform is dynamically adjusted to

$$\hat{V}_p = \begin{cases} V_p - \delta V & \text{when } V_p - \delta V > V_{\min} \\ V_{\min} & \text{when } V_p - \delta V \le V_{\min} \end{cases}, \tag{24}$$

where $V_{\min}$ is introduced to saturate the dynamic adjustment to make sure that the printing velocity is not too slow. The velocity control procedure is illustrated in FIGURE 3.

The thermoplastic matrix material extrusion lengths are assumed to be proportional to the curve length and given by

$$L_m = \beta_m s, \tag{25}$$

where β_f represent the extrusion rate ratio of matrix.

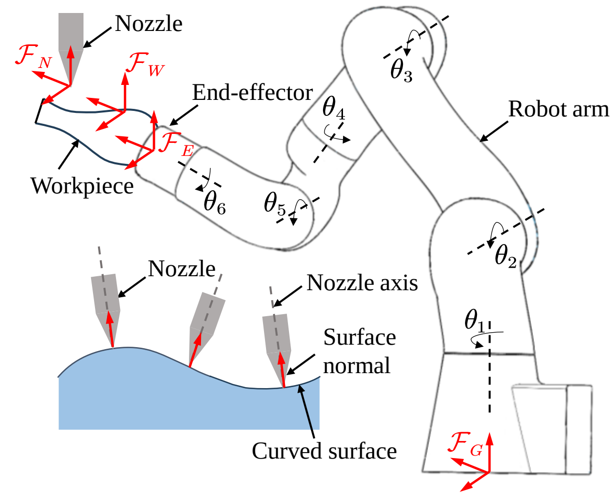

FIGURE 2: SCHEMATICS OF A ROBOT-BASED MULTI-AXIS CFRP-AM SYSTEM AND FIBER DEPOSITION DIRECTION

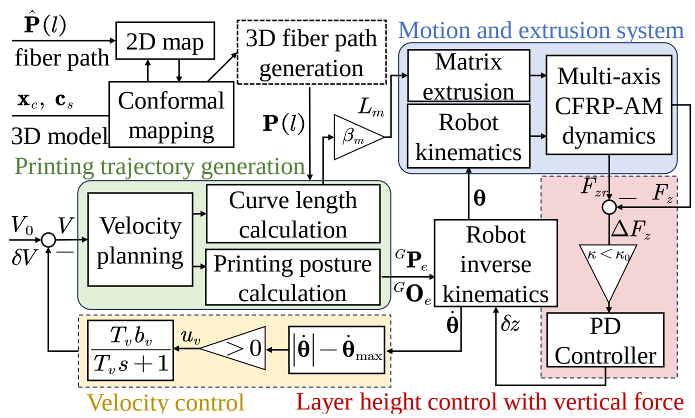

FIGURE 3: BLOCK DIAGRAM OF THE CLOSED-LOOP FEEDBACK CONTROL OF THE MULTI-AXIS CFRP-AM PROCESS

3. CONTACT FORCE BASED CLOSED-LOOP CONTROL OF MULTI-AXIS CFRP-AM PROCESS ON CONCAVE SURFACE

3.1. Printing faults analysis on concave surface

According to FIGURE 4, for a point $\mathbf{P}_f$ of the fiber path on the complex surface, define $\boldsymbol{\alpha}$ and $\boldsymbol{\beta}$ are the tangent and normal vector of fiber path at that location, $\mathbf{n}$ and $\mathbf{v}$ are the tangent vector and normal vector of the surface at that point, respectively. The curvature κ of the fiber path at point $\mathbf{P}_f$ is defined as

$$\kappa = |d\mathbf{P}/ds|, \tag{26}$$

which can be divided into two parts by

$$\kappa = \kappa_g \mathbf{v} + \kappa_n \mathbf{n}, \tag{27}$$

where κ_g and κ_n are the geodesic curvature and normal curvature of the surface. The contact force on the fiber at point $\mathbf{P}_f$ is $\mathbf{F}$, which is divided to

$$\begin{cases} \mathbf{F}_n + \mathbf{F}_t = \mathbf{F}\kappa_g \mathbf{v} \\ \mathbf{F}_z = \mathbf{F}\kappa_n \mathbf{n} \end{cases}, \tag{28}$$

where $\mathbf{F}_t$, $\mathbf{F}_n$, and $\mathbf{F}_z$ represents the tangential, side, and vertical forces, respectively. $\mathbf{F}_t$ and $\mathbf{F}_n$ are the forces that cause the fiber to slide on the surface and $\mathbf{F}_z$ is the force that influence the bonding between fiber and surface. The $\mathbf{F}_t$ and $\mathbf{F}_n$ are mainly dependent on the fiber path shape $\hat{\mathbf{P}}$ defined in the 2D plane. The large curvatures of fiber path, like sharp corner regions, will cause large $\mathbf{F}_t$ and $\mathbf{F}_n$, and lead to fiber slippages. The $\mathbf{F}_z$ is mainly determined by the surface normal curvature κ_n and fiber path orientation on the surface. According to Euler's formula,

$$\kappa_n = \kappa_u \cos^2\varphi + \kappa_v \sin^2\varphi, \tag{29}$$

where κ_u and κ_v are two principal curvatures of the surface, and φ is the angle between the fiber tangential direction and plane direction of κ_u. It has $\kappa_n < 0$ when the surface is a concave surface. When the $\mathbf{F}_z$ is insufficient, it will lead to weak bonding between fiber and surface and results in fiber bridge when passing concave regions. On the contrary, overlarge $\mathbf{F}_z$ causes over compression and fiber abrasion.

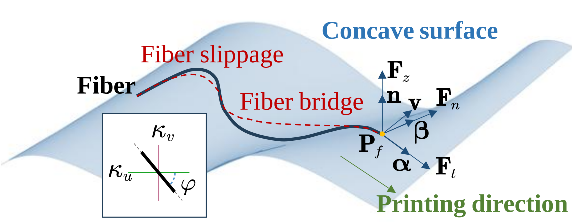

FIGURE 4: SCHEMATICS OF FIBER ON CONCAVE SURFACE AND REPRESENTATIVE FAULTS

3.2. Contact-force-based closed-loop controller

The fiber contact force is a representative monitoring signal for the printing quality. For the fiber material with large stiffness, especially for fiber prepreg, the $\mathbf{F}_t$ and $\mathbf{F}_n$ behave larger when the fiber is deformed. The potential to occur fiber slippages is higher. For the fiber material with relatively small stiffness, such as dry fiber, the fiber deformation causes smaller $\mathbf{F}_t$ and $\mathbf{F}_n$. The force feedback controller incorporating $\mathbf{F}_t$, $\mathbf{F}_n$, and $\mathbf{F}_z$ has been investigated and proved efficient in our previous research under the 2D scenario. Here for the multi-axis CFRP-AM process, to simplify the problem, the dry fiber is adopted for printing to minimize the $\mathbf{F}_t$ and $\mathbf{F}_n$'s influence on fiber deposition accuracy. The vertical force $\mathbf{F}_z$ is focused on to address fiber bridge defects when printing on complex surfaces with concave features.

The vertical contact force $\mathbf{F}_z$ during the printing process directly reflects the bonding condition between newly deposited continuous fiber and the printing surface. The unsuitable $\mathbf{F}_z$ will cause printing defects like fiber bridge and abrasion. According to the multi-axis printer configuration described in Section 2.3, the local surface's normal direction is always aligned with the vertical build orientation, which means the orientation of $\mathbf{F}_z$ is constant and its value $F_z = |\mathbf{F}_z|$. The F_z can be exploited as feedback signals for closed-loop control by dynamically adjusting the height between nozzle and surface. To maintain a relatively stable contact force reference value, the vertical force error can be defined by

$$\Delta F_z = \begin{cases} F_{zr} - F_z & \text{when } \kappa_g \le \kappa_0 \\ 0 & \text{when } \kappa_g > \kappa_0 \end{cases}, \tag{30}$$

where κ_g is the curvature in the current printing trajectory and κ_0 is its adjustment upper limit. The measurement indicates that the vertical force error signal is only recorded at low-curvature regions to adjust the layer height. This choice arises from the CFRP-AM process characteristics exhibiting significant force patterns around the high-curvature regions. The irregular vertical force is due to the uneven surface at the high-curvature region caused by high fiber stiffness. Therefore, the layer height adjustment should avoid such regions.

The vertical force error signal is converted to the dynamic adjustment of the height between nozzle and printing surface through a proportional-derivative (PD) controller given by

$$\delta z_0 = K_p \Delta F_z + K_d \frac{d\Delta F_z}{dt},$$

$$\delta z = \begin{cases} \delta z_{\max} & \text{when } \delta z_0 > \delta z_{\max} \\ \delta z_{\min} & \text{when } \delta z_0 < \delta z_{\min} \\ \delta z_0 & \text{elsewhere} \end{cases}. \tag{31}$$

where K_p and K_d are proportional and derivative coefficients, respectively. To avoid huge displacement of the motion platform, the saturation limitation is added to the δz, and $\delta_{\min}$, $\delta_{\max}$ are the lower and upper saturation limits, respectively. The modified z position for the robot end-effector becomes

$$\hat{P}_{ez}(t) = P_{ez}(t) + \int \delta z\, dt\,. \tag{32}$$

An event trigger $(s(t) \geqslant s_f)$ is added to the dynamic control process to mark the completion of the printing. The overall block diagram of the closed-loop feedback control of the multi-axis CFRP-AM process is illustrated in FIGURE 3.

4. EXPERIMENTS

4.1. Experimental Setup

A robotic-based multi-axis CFRP-AM system, shown in FIGURE 5, is designed and built as the experimental platform for this study. An industrial 6-axis industrial robot (Huashu Co603), a self-designed continuous fiber and thermoplastic co-extrusion system, and a load cell (Hypersen HPS-FT060E) are integrated and controlled with Beckhoff TWINCAT real-time control system with EtherCAT communication and 1 kHz sampling rate. A print base with complex surface is printed by the commercial 3D printer (Creality K1 Max) using PLA filament and connected to the end-effector of industrial robot before printing. The reference printing trajectory is then generated based on the conformal-mapping-based method shown in Section 2. The trajectory generation algorithm is implemented in MATLAB on a PC with an i5-13500HX CPU with less than 5 seconds for the surface containing 48000 points.

During the printing process, the extruder and load cell are fixed, and the industrial robot and print base move to execute the joint space trajectory $\mathbf{\Theta}$. The velocity controller is applied to ensure the joint angle velocity $\dot{\mathbf{\Theta}}$ is always in safe condition. The detailed control parameters are shown in TABLE 2. The continuous fiber adopted is continuous dry basalt fiber, which is soft compared to fiber prepreg. The fiber roll is placed on an automatic turntable to ensure that it is relaxed before entering the extruder. The dry basalt fiber is threaded through the nozzle before printing. During the printing process, the matrix filament is fed by a stepper motor with length L_m and melts in the heated chamber. The dry fiber is impregnated with melted resin, adheres to the print base, and drags the subsequent fiber out. The nozzle temperature keeps 210 °C to melt the matrix PLA. To ensure the load cell is at its safe operating temperature of <50 °C, a quartz heat insulation panel is set between the heated extruder and load cell. The load cell measures the 3-axis contact force of the CFRP-AM process. The connector linking the contact point and the load cell is characterized by rigidity, ensuring that the forces measured by the load cell accurately correspond to the forces exerted at the contact point. This validation has been confirmed through a preliminary test. The raw force signals obtained from the load cell are processed with zero calibration and median filtering and are concatenated into a vector $\mathbf{F}$. The measurement is converted to the tangential, side, and vertical forces by Eq.(28) in Section 3.2. The detailed CFRP-AM system parameters are listed in TABLE 1.

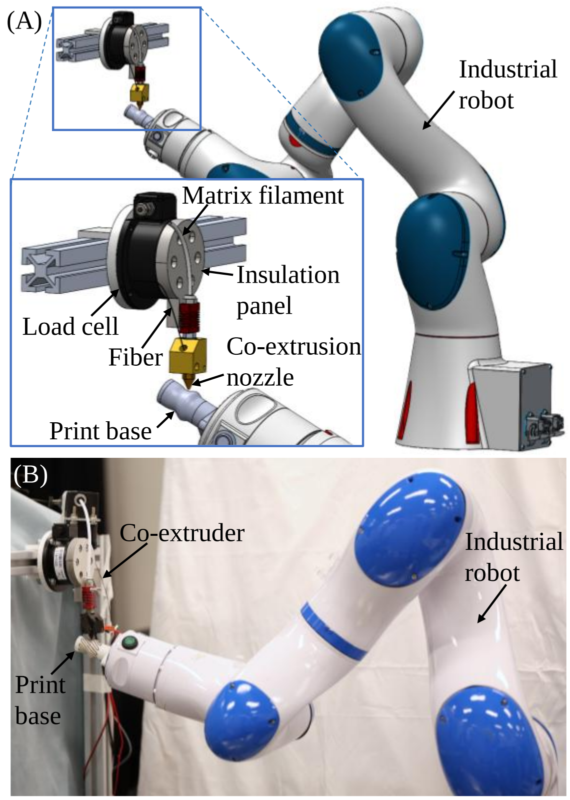

FIGURE 5: (A) SCHEMATICS AND (B) PHOTO OF MULTI-AXIS CFRP-AM EXPERIMENTAL SETUP

TABLE 1: PARAMETERS OF ROBOTIC-BASED MULTI-AXIS CFRP-AM PLATFORM

Parameter	**Values**
Nozzle diameter	0.8 mm
Matrix material	Polylactic acid (PLA)
Continuous fiber	Dry basalt fiber-0.4K
Nozzle temperature	210 °C
Fiber printing velocity	1~10 mm/s
Sampling time t_s	0.001 s

TABLE 2: PARAMETERS OF VELOCITY CONTROLLER

Parameters	Values
$\dot{\mathbf{\Theta}}_{\max}$	[30, 30, 30, 30, 30, 30] (°)
T_v	1 (s)
b_v	1
$V_{\min}$	0.5 (mm/s)

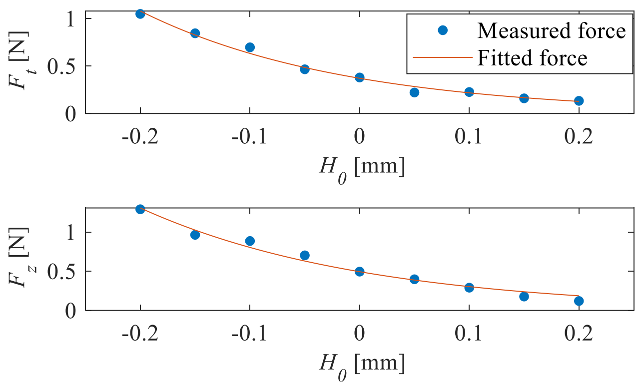

FIGURE 6: RELATIONSHIP BETWEEN LAYER HEIGHT AND CONTACT FORCES

4.2. Vertical contact force with printing parameters

To identify the influence of distance between nozzle and print base (layer height) h_0 on the contact forces, a series of open-loop printing experiments were performed, and the results are summarized in FIGURE 6. The valid testing layer height varies from -0.2 mm (where fiber abrasion occurs) to 0.2 mm (where bonding failure occurs). The fibers are deposited on a cylinder with a zigzag path, and the average force at straight regions is selected for data fitting. Since the fiber path is straight, the normal force F_n is close to zero and not considered. The fitted tangential and vertical contact forces formulate a nonlinear function as shown in FIGURE 6. The fitted functions are expressed as $F_t = Ae^{Bh_0}$ and $F_z = Ce^{Dh_0}$, with parameters $A = 0.371$, $B = -5.343$, $C = 0.494$, and $D = -4.865$. The R^2 of the fits are more than 95%, indicating a desirable estimation. Exponential decay of the contact forces regarding the layer height is observed. To avoid fiber abrasion and detachment, the contact force 0.6 N, which is in the middle region, is selected as the reference force F_{zr} for feedback control.

4.3. Vertical contact force control verification

A revolution part with concave surface, as shown in FIGURE 7, is exploited to evaluate the performance with layer height CL control. The parts were printed with parameters in TABLE 3 and shown in FIGURE 9. The printed parts were put into a mold and filled with epoxy to protect the deposited fiber shape on the curved surface. After curing, the parts were cut at two cutting planes $\mathscr{C}_1$ and $\mathscr{C}_2$ with representative concave surface regions shown in FIGURE 7 (B). The cut surfaces are sanded, polished, and captured by a camera. The black fiber and white printing surface can be segmented after image processing. The printing surface is represented by a circle with center $\mathbf{P}_c$ and radius r_s. The point closest to the printing surface of each fiber bundle is defined as $\mathbf{P}_b$. The fiber bridge is evaluated by the distance between $\mathbf{P}_b$ and printing surface, known as e_b, and calculated by

$$e_b = \|\mathbf{P}_b - \mathbf{P}_c\| - r_s. \tag{33}$$

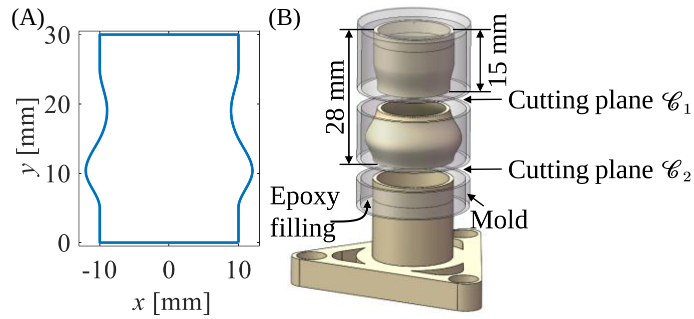

FIGURE 7: (A) 2D AND (B) 3D SHAPES OF PRINT PART WITH CONCAVE SURFACE, AND FIBER BRIDGE EVALUATION SCHEMATICS

TABLE 3: PRINTING AND CONTROL PARAMETERS

Parameters	h_0	V_p	β_m	K_p, K_d	$\delta_{\min}, \delta_{\max}$
Values	0.2 [mm]	2 [mm/s]	0.2 -	0.1,0.1 [mm]	-0.2, 0.2 [mm]

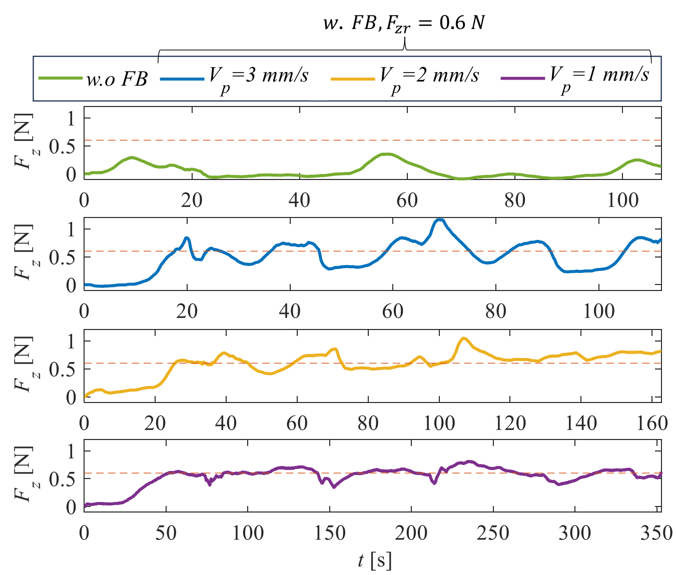

FIGURE 8: FORCE SIGNAL TIME HISTORY DURING PRINTING WITHOUT (W.O.) AND WITH (W.) FEEDBACK (FB) CONTROL UNDER DIFFERENT VELOCITY

The vertical contact force shown in FIGURE 8 illustrates that the overall vertical force is at a relatively low value and exhibits significant fluctuations. When printing on the convex regions of the surface, the force is higher, while it is lower at concave regions. This is due to various reasons such as unreasonable layer height and tracking error of the robot arm due to complex movement trajectory, etc. The low vertical force value indicates a relatively weak adhesion of deposited fiber, raising the risk of printing defects. In contrast, with the application of feedback control, the vertical contact force is maintained around the reference force during the entire printing process, indicating an enhanced level of adhesion. To analyze quantitatively, the average vertical force, its error to the desired force, and its standard deviation (SD) are calculated and presented in TABLE 4. The average forces and force error prove that the actual vertical forces are successfully controlled around the desired value when the feedback control is applied. The control efficiency is reasonable under different printing velocities. However, the SD increases with the increase in printing velocity. In summary, the controller exhibits the best performance when the printing velocity is 1 mm/s, though its efficiency becomes relatively attenuated when the velocity increases.

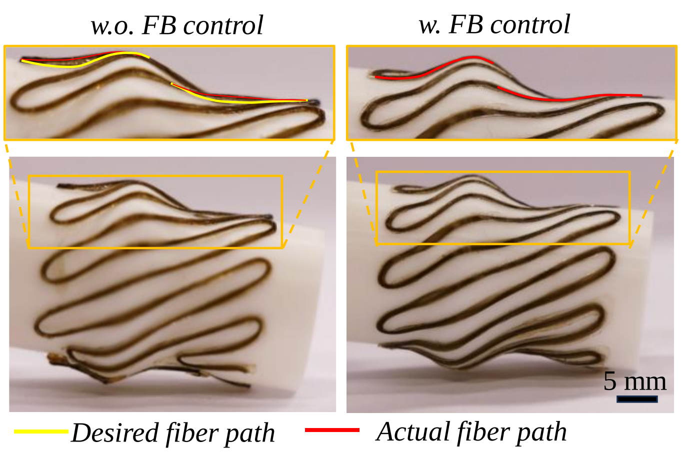

FIGURE 9: PRINTED RESULTS WITHOUT (W.O.) AND WITH (W.) FEEDBACK (FB) CONTROL

TABLE 4: OVERALL EVALUATION OF FORCE SIGNAL DURING PRINTING WITHOUT (W.O.) AND WITH (W.) FEEDBACK (FB) CONTROL UNDER DIFFERENT VELOCITY

Test		Actual force (N)			Desired force (N)
		Average force	Average force error	SD	
w.o. FB		0.054	0.946	0.133	-
w. FB, V_p (mm/s)	1	0.587	0.013	0.088	0.6
	2	0.600	0.000	0.128	
	3	0.675	0.075	0.245	

The printouts without and with FB control are shown in FIGURE 9. It is obvious that the printed part without feedback control shows fiber bridges at concave surface regions. When fiber deposits on a concave surface with large curvature, the tension on the fiber facilitates its recovery to the straight path. The weak adhesion between the fiber and the printing surface is insufficient to retain the tensioned fiber, resulting in fiber detachment, a phenomenon known as a fiber bridge, which is marked by red curves shown in FIGURE 9. When the feedback control is introduced, the fibers are sufficiently adhered to the print surface and no fiber bridges are found shown in FIGURE 9. When analyzing the cross-sections of concave regions shown in FIGURE 10, it can be seen the e_b of the printout without feedback control is 0.865 mm and 0.860 mm at cutting planes $\mathscr{C}_1$ and $\mathscr{C}_2$, respectively. For the printout with FB control, fibers are located on the print surface with a maximum offset e_b of 0.272 mm and 0.185 mm at $\mathscr{C}_1$ and $\mathscr{C}_2$, respectively. The elimination of fiber bridges at concave surfaces demonstrates the effectiveness of vertical force feedback control.

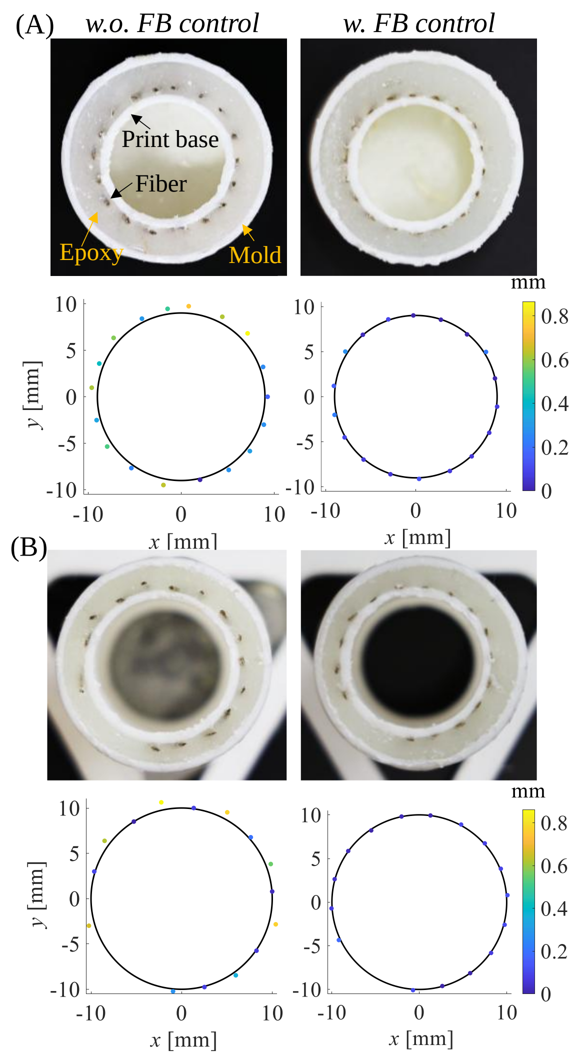

FIGURE 10: FIBER BRIDGE EVALUATION AT CONCAVE REGIONS. CUTTING PLANES (A) $\mathscr{C}_1$ AND (B) $\mathscr{C}_2$

5. CONCLUSION

This paper proposed a contact-force-based closed-loop-controlled multi-axis CFRP-AM system enabling printing on complex surfaces with concave regions. To generate a multi-axis printing trajectory, a conformal-mapping-based method is proposed to design fiber paths in a 2D plane and angle-preserved transform them into executable printing trajectories for the multi-axis printing system. To improve printing quality on complex surfaces, real-time vertical contact force during the printing process is exploited for feedback control by dynamically adjusting the layer height. A revolution part with concave surfaces is printed to verify the proposed method. Fiber bridges at concave regions are efficiently reduced with the application of feedback control, showing a significant improvement effect.

ACKNOWLEDGEMENTS

The authors acknowledge support from the Research Grants Council (RGC) of the Government of Hong Kong Special Administrative Region (HKSAR) with RGC/ECS Project (No. 26215824), HKUST research equipment development fund, and HKUST Bridge Gap Fund (BGF). This work was supported in part by the Project of Hetao Shenzhen-Hong Kong Science and Technology Innovation Cooperation Zone (HZQB-KCZYB-2020083). The help from the funding agency and the other researchers is sincerely appreciated.

REFERENCES

[1] Goh, G. D., Toh, W., Yap, Y. L., Ng, T. Y., and Yeong, W. Y., 2021, "Additively Manufactured Continuous Carbon Fiber-Reinforced Thermoplastic for Topology Optimized Unmanned Aerial Vehicle Structures," Compos B Eng, **216**, p. 108840. https://doi.org/10.1016/j.compositesb.2021.108840.

[2] Wang, X., Jiang, M., Zhou, Z., Gou, J., and Hui, D., 2016, "3D Printing of Polymer Matrix Composites: A Review and Prospective," Compos B Eng, **110**. https://doi.org/10.1016/j.compositesb.2016.11.034.

[3] Li, N., Li, Y., and Liu, S., 2016, "Rapid Prototyping of Continuous Carbon Fiber Reinforced Polylactic Acid Composites by 3D Printing," J Mater Process Technol, **238**, pp. 218–225. https://doi.org/10.1016/j.jmatprotec.2016.07.025.

[4] Chen, R., Bratten, A., Rittenhouse, J., Leu, M. C., and Wen, H., 2023, "Additive Manufacturing of Continuous Carbon Fiber-Reinforced SiC Ceramic Composite with Multiple Fiber Bundles by an Extrusion-Based Technique," Ceram Int, **49**(6), pp. 9839–9847. https://doi.org/https://doi.org/10.1016/j.ceramint.2022.11.157.

[5] Cheng, P., Peng, Y., Li, S., Rao, Y., Le Duigou, A., Wang, K., and Ahzi, S., 2023, "3D Printed Continuous Fiber Reinforced Composite Lightweight Structures: A Review and Outlook," Compos B Eng, **250**(November 2022), p. 110450. https://doi.org/10.1016/j.compositesb.2022.110450.

[6] Liu, G., Xiong, Y., and Zhou, L., 2021, "Additive Manufacturing of Continuous Fiber Reinforced Polymer Composites: Design Opportunities and Novel Applications," Composites Communications, **27**. https://doi.org/10.1016/j.coco.2021.100907.

[7] Chen, X., Fang, G., Liao, W., and Wang, C. C. L., 2021, "Field-Based Toolpath Generation for 3D Printing Continuous Fibre Reinforced Thermoplastic Composites."

[8] Ruan, J., Sparks, T. E., Panackal, A., Liou, F. W., Eiamsa-Ard, K., Slattery, K., Chou, H.-N., and Kinsella, M., 2007, "Automated Slicing for a Multiaxis Metal Deposition System," J Manuf Sci Eng, **129**(2), pp. 303–310. https://doi.org/10.1115/1.2673492.

[9] de Backer, W., van Tooren, M. J. L., and Bergs, A. P., 2018, "Multi-Axis Multi-Material Fused Filament Fabrication with Continuous Fiber Reinforcement," *AIAA/ASCE/AHS/ASC Structures, Structural Dynamics, and Materials Conference, 2018*, American Institute of Aeronautics and Astronautics Inc, AIAA. https://doi.org/10.2514/6.2018-0091.

[10] Zhang, K., Zhang, W., and Ding, X., 2020, "Multi-Axis Additive Manufacturing Process for Continuous Fibre Reinforced Composite Parts," *Procedia CIRP*, Elsevier B.V., pp. 113–117. https://doi.org/10.1016/j.procir.2019.09.022.

[11] Yao, Y., Cheng, L., and Li, Z., 2024, "A Comparative Review of Multi-Axis 3D Printing," J Manuf Process, **120**, pp. 1002–1022. https://doi.org/10.1016/j.jmapro.2024.04.084.

[12] Wu, Q., Zu, L., Zhang, Q., Zhang, G., Chen, S., Wang, H., Li, D., and Liu, H., 2022, "Filament Winding Analysis and Experimental Verification of a Combined Revolution Body with a Concave Surface," Compos Struct, **280**. https://doi.org/10.1016/j.compstruct.2021.114951.

[13] Xie, F., Chen, L., Li, Z., and Tang, K., 2020, "Path Smoothing and Feed Rate Planning for Robotic Curved Layer Additive Manufacturing," Robot Comput Integr Manuf, **65**. https://doi.org/10.1016/j.rcim.2020.101967.

[14] Chen, S., Yang, Y., Liu, S., and Duan, M., 2023, "In-Situ Additive Manufacturing Deposition Trajectory Monitoring and Compensation with Thermal Camera," Addit Manuf, **78**, p. 103820. https://doi.org/https://doi.org/10.1016/j.addma.2023.103820.

[15] Mercado, F., and Rojas Arciniegas, A., 2020, "Additive Manufacturing Methods: Techniques, Materials, and Closed-Loop Control Applications," The International Journal of Advanced Manufacturing Technology, **109**. https://doi.org/10.1007/s00170-020-05663-6.

[16] Lu, L., Hou, J., Yuan, S., Yao, X., Li, Y., and Zhu, J., 2023, "Deep Learning-Assisted Real-Time Defect Detection and Closed-Loop Adjustment for Additive Manufacturing of Continuous Fiber-Reinforced Polymer Composites," Robot Comput Integr Manuf, **79**, p. 102431. https://doi.org/10.1016/j.rcim.2022.102431.

[17] Yang, Y., Zhou, Y., and Duan, M., 2024, "Contact-Force-Based Closed-Loop Control of Shell Structure Additive Manufacturing with Continuous-Fiber-

Reinforced Polymer Composites," J Mater Process Technol, p. 118501. https://doi.org/https://doi.org/10.1016/j.jmatprotec.2024.118501.
[18] Lee, W. Il, and Springer, G. S., 1987, "A Model of the Manufacturing Process of Thermoplastic Matrix Composites," J Compos Mater, **21**(11), pp. 1017–1055. https://doi.org/10.1177/002199838702101103.
[19] Zhang, Z., Long, Y., Yang, Z., Fu, K., and Li, Y., 2022, "An Investigation into Printing Pressure of 3D Printed Continuous Carbon Fiber Reinforced Composites," Compos Part A Appl Sci Manuf, **162**(June), p. 107162. https://doi.org/10.1016/j.compositesa.2022.107162.
[20] De Backer, W., Sinkez, P., Chhabra, I., Van tooren, M., and Bergs, A., 2020, *In-Process Monitoring of Continuous Fiber Additive Manufacturing through Force/Torque Sensing on the Nozzle*. https://doi.org/10.2514/6.2020-1632.
[21] Zhou, Y., Gao, L., and Li, H., 2022, "Graded Infill Design within Free-Form Surfaces by Conformal Mapping," Int J Mech Sci, **224**. https://doi.org/10.1016/j.ijmecsci.2022.107307.
[22] Meng, T. W., Choi, G. P. T., and Lui, L. M., 2016, "TEMPO: Feature-Endowed Teichmüller Extremal Mappings of Point Clouds," SIAM J Imaging Sci, **9**(4), pp. 1922–1962. https://doi.org/10.1137/15M1049117.
[23] Wang, S., Wang, Y., Jin, M., Gu, X. D., and Samaras, D., 2007, "Conformal Geometry and Its Applications on 3D Shape Matching, Recognition, and Stitching," IEEE Trans Pattern Anal Mach Intell, **29**(7), pp. 1209–1220. https://doi.org/10.1109/TPAMI.2007.1050.
[24] He, S., Ma, P.-C., and Duan, M., 2024, "Continuous Fiber Path Optimization in Additive Manufacturing: A Gradient-Based B-Spline Finite Element Approach," Addit Manuf, **86**, p. 104155. https://doi.org/10.1016/j.addma.2024.104155.

